Uncoupled Digital Radars Creating a Coherent Sensor Network

JULIAN AGUILAR (Graduate Student Member, IEEE),
DAVID WERBUNAT (Graduate Student Member, IEEE),
VINZENZ JANOUDI (Graduate Student Member, IEEE), **CHRISTINA BONFERT** (Member, IEEE),
AND CHRISTIAN WALDSCHMIDT (Fellow, IEEE)

(Regular Paper)

Institute of Microwave Engineering, Ulm University, 89081 Ulm, Germany

CORRESPONDING AUTHOR: Julian Aguilar (e-mail: julian.aguilar@uni-ulm.de).

ABSTRACT   Radar networks offer the possibility to overcome the limitations of single sensors. However, without coherent signal processing, the full potential of radar networks cannot be exploited. Therefore, the synchronization of independent radar sensors is crucial in order to mitigate performance degradation due to frequency deviations of uncoupled reference oscillators. Systematically derived synchronization criteria for coupling-induced errors such as sampling frequency offset (SFO), carrier frequency offset (CFO) and symbol timing offset (STO) of uncoupled orthogonal frequency-division multiplexing (OFDM) radar sensors enable to determine hardware specifications, such as the required reference oscillator frequency stability. This aids in the design of digital radar networks and ensures error-free signal processing in advance. The concept of deriving said criteria is applicable to other modulation types used for digital radar sensors. Additionally, signal processing-based error estimation and correction methods are presented. By exploiting standard radar images, namely range profiles and range-Doppler images, the proposed methods estimate and correct any occurring SFO, CFO and STO. Furthermore, by applying the signal processing synchronization methods, they allow for a more lenient radar network design. Measurements using a 77 GHz digital radar demonstrator verify the derived criteria and error estimation and correction methods.

INDEX TERMS   Bistatic, carrier frequency offset (CFO), digital radar, multistatic, OFDM radar, phase noise, radar network, sampling frequency offset (SFO), symbol timing offset (STO), synchronization, timing recovery.

I. INTRODUCTION

Radar sensors play a crucial role in various applications, spanning from automotive [1], remote sensing [2], and joint communication and sensing (JCAS) [3], [4] to medicine [5], among others. The increasing adoption of radar technology across diverse domains introduces new performance demands, particularly for high-resolution radar imaging. However, achieving high resolution direction of arrival (DoA) estimation is constrained by the size limitations of the radar aperture and sensor.

One way to overcome the limitations of a single multiple-input multiple-output (MIMO) sensor is a radar network [6], [7], [8], comprising multiple cooperative sensor nodes. In this way, radar networks offer the possibility to extend the network aperture beyond the one of a single radar and enable imaging based on the combined aperture of multiple sensors [8]. While radar network approaches without the need for coherent signal evaluation exist [9], [10], the full potential of radar networks requires time, frequency and phase coherency between radar nodes, which allows the exploitation of multistatic signal processing [11], [12]. This makes techniques such as network-based DoA estimation [13] and multistatic synthetic aperture radar (SAR) [14], [15] feasible.

Various synchronization strategies have been proposed to achieve coherency in radar networks. While it is possible to distribute the radio frequency (RF) signal to multiple radar

frontends [16] (RF coupled network), this has the drawback of costly and complex hardware. Alternatively, low frequency (LF) coupled networks [11], [17] distribute a reference oscillator (REF) signal instead of the RF signal, offering reduced complexity and costs compared to RF-coupled topologies. Nonetheless, LF-coupled networks still require a distribution network for the REF signal, limiting the network's flexibility.

Recent research has demonstrated that completely uncoupled radar networks can also achieve coherency. In [18], a frequency modulated continuous wave (FMCW) radar network is proposed, relying on tuned REF sources and digital signal processing to correct remaining frequency offsets. This way, network-based DoA estimation is feasible. Furthermore, [19] exploits the capabilities of digital radars by recovering coherency in a network of phase-modulated continuous wave (PMCW) radars. Through digital signal processing at the receiver, errors due to SFO, CFO, and phase noise are mitigated.

The aim of this work is to analyse the coupling-induced errors of an uncoupled OFDM radar network and the coherency required for subsequent signal processing. By gaining knowledge of the level of synchronization needed for coherent signal processing, the design of radar networks can be optimised. Initially, a detailed signal model for uncoupled OFDM radars is derived, followed by a comprehensive analysis of the errors caused by an uncoupled network topology. This analysis encompasses the effects caused by incoherent RF carriers as well as by uncoupled digital-to-analog converter (DAC) and analog-to-digital converter (ADC) sampling clocks. Through this approach, a detailed study is provided, enabling the assessment of the sensing capabilities of an uncoupled OFDM radar network and its dependencies on the OFDM parameters. While this paper uses the OFDM modulation scheme as an example, most of the procedure steps are applicable to other modulation types used for digital radars.

Consequently, criteria in terms of maximum frequency and time deviations are calculated. These criteria are used to estimate the required frequency stability of sampling clocks and local oscillators (local oscillator (LO)), as well as the frame trigger stability. Furthermore, error estimation and correction algorithms are presented. The proposed algorithms are independent of the modulation type and are applied to range-Doppler data. To verify the aforementioned criteria as well as the error estimation and correction algorithms, measurements are performed at 77 GHz. The measurement setup used allows for low frequency coupling and uncoupled measurements, enabling a detailed examination of coupling-induced errors as well as the performance of estimation and correction methods.

The paper is divided into three thematic parts, where all parts contain theory and measurements. The first part introduces the signal model and coupling-induced errors. To do so, Section II provides a detailed mathematical description of a bistatic OFDM radar channel, as well as a standard range-Doppler estimation scheme. Afterwards, Section III offers a description of the measurement setup used for validation. In the second part, criteria are derived to minimize the effect of coupling-induced errors on range-Doppler estimation. For this, in the following three sections the aforementioned errors are separately analysed and measurements conducted. Section IV does this for an SFO, while Section V contains the derivations and measurements for a CFO. In Section VI, said criteria and measurements for an STO are found. Finally, part three introduces the error estimation and correction methods, which can be found in Section VIII.

II. SIGNAL MODEL

To reduce complexity, the requirements on synchronization are derived using a single bistatic channel with uncoupled REF. In the context of this paper, a bistatic channel is a single virtual channel of independent transmit (Tx) and receive (Rx) sensors. This derivation is sufficient, since the coupling induces errors affect all bistatic channels between the same Tx and Rx pair equally. For a large network with multiple radar sensors, the following equations and synchronization requirements must be computed for all sensor pairs.

In practice, all frequencies and clocks that are needed for the signal synthesis are usually derived from one REF. For a general description of network synchronization errors, these signals are separated and therefore independently analysed.

A. MODULATION & PROPAGATION

The complex envelope of the mth OFDM symbol with duration T of a OFDM system in time-domain is described by [20]

$$x_m(t) = \text{IDFT}(D_{m,\text{Tx}})_n$$
$$= \sum_{n=0}^{N-1} d_{mn}e^{j2\pi n\Delta ft}, \ t \in [0, T), \tag{1}$$

where $\text{IDFT}(D_{m,\text{Tx}})_n$ is the Inverse Discrete Fourier Transform (IDFT) of the mth row of the Tx symbol matrix $D_{\text{Tx}} \in \mathbb{C}^{M\times N}$ with elements $d_{mn} \in D_{\text{Tx}}$, $N \in \mathbb{N}$ the number of subcarriers, $n = 0, \ldots, N-1$ the discrete subcarrier index, $M \in \mathbb{N}$ the number of transmitted OFDM symbols, $m = 0, \ldots, M-1$ the symbol index and $\Delta f = \frac{1}{T}$ the subcarrier spacing with symbol duration T. Usually a cyclic prefix (CP), which is a copy of (1) with duration $T_{\text{CP}} < T$, is added to the beginning of each symbol to artificially create a pseudo periodic time-domain signal. The CP is removed at the receiver and if its length is sufficiently long, interference between consecutive OFDM symbols (intersymbol interference (ISI)) caused by long channel delays is avoided.

To simplify the mathematical expressions, all path losses, noise contributions, phase noise (PN) and CP samples are neglected. Furthermore, the transmitter is, without loss of generality, assumed to be ideal, i.e. without coupling-induced errors, while the receivers REF could deviate from the intended frequency. Therefore, the carrier frequency (CF) of the transmitters LO is $f_{\text{c,Tx}} = f_{\text{c}}$. After upconversion using the transmitters LO, (1) becomes

$$x_m^{\text{RF}}(t) = x_m(t)e^{j2\pi f_{\text{c}}t}$$

$$= \sum_{n=0}^{N-1} d_{mn} e^{j2\pi(n\Delta f + f_c)t}. \tag{2}$$

In the channel the transmitted OFDM symbol is reflected from a target at range R and scattered back to the Rx channel. The time-of-flight τ is well approximated by

$$\tau(t) = \tau_R + \tau_v(t) \approx \frac{2R}{c_0} + \frac{2v}{c_0}t, \tag{3}$$

with c_0 the speed of light and v the target's radial velocity. Therefore, the mth OFDM receive symbol for a single point target is

$$y_m^{RF}(t) = x_m^{RF}(t - \tau(t))$$
$$= \sum_{n=0}^{N-1} d_{mn} e^{j2\pi(n\Delta f + f_c)(t - \tau(t))}. \tag{4}$$

Subsequently, the downconversion of (4) to baseband at the receive channel is performed using a possibly faulty CF $f_{c,Rx} = \delta_c f_c$, where the CFO is given by $f_{CFO} = (1 - \delta_c)f_c$, $\delta_c \in \mathbb{R}^+$. The received signal after downconversion can be written as

$$y_m(t) = y_m^{RF}(t) e^{-j2\pi\delta_c f_c t}$$
$$= \sum_{n=0}^{N-1} d_{mn} e^{j2\pi n\Delta f t} e^{j2\pi(1-\delta_c)f_c t}$$
$$\times e^{-j2\pi(n\Delta f + f_c)\tau(t)}. \tag{5}$$

B. SAMPLING OF THE RECEIVED SIGNAL

Before demodulation and range-Doppler estimation, the received signal (5) has to be sampled using the receiver's ADC. As the sampling clocks of the transmitter's DAC, which is $f_{s,Tx} = f_s$, and the receiver's ADC are not coupled, the receiver's ADC clock, which is $f_{s,Rx} = \delta_s f_s$, is offset by an SFO of $f_{SFO} = (1 - \delta_s)f_s$. Thus, the discrete time after sampling becomes dependent on δ_s. In general, the sampling points during one OFDM symbol can be described by $\frac{k}{f_s}$, $k \in \mathbb{N}_0 \cap k = 0, \ldots, \lfloor T f_s \rfloor$, k the sample index, and the time offset of the mth symbol by $m\frac{N}{f_s}$. Subsequently, the discrete-time receive signal becomes

$$y_m[k] = y_m\left(\frac{k}{\delta_s f_s} + m\frac{N}{\delta_s f_s}\right)$$
$$= \sum_{n=0}^{N-1} d_{mn} e^{j2\pi n\Delta f\left(\frac{k}{\delta_s f_s} + m\frac{N}{\delta_s f_s}\right)}$$
$$\times e^{j2\pi(1-\delta_c)f_c\left(\frac{k}{\delta_s f_s} + m\frac{N}{\delta_s f_s}\right)}$$
$$\times e^{j2\pi(n\Delta f + f_c)\tau[k]}, \tag{6}$$

with the discrete time of travel

$$\tau[k] = \frac{2R}{c_0} + \frac{2v}{c_0}\left(\frac{k}{\delta_s f_s} + m\frac{N}{\delta_s f_s}\right). \tag{7}$$

C. DEMODULATION

To obtain the received symbols $D_{Rx} \in \mathbb{C}^{M \times N}$, a Discrete Fourier Transform (DFT) of the discrete-time receive signal (6) is performed via

$$D_{m,Rx} = \text{DFT}(y_m[k])_l$$
$$= \frac{1}{N} \sum_{k=0}^{N-1} y_m[k] e^{-j2\pi l\Delta f\left(\frac{k}{f_s} + m\frac{M}{f_s}\right)}, \tag{8}$$

where $l = 0, \ldots, N - 1$ is the discrete subcarrier index, i.e. the spectral components of y. Without any coupling related errors, i.e. $\delta_c = \delta_s = 1$, the IDFT and DFT used for signal modulation and demodulation cancel each other out such that $D_{m,Rx} \neq 0 \, \forall n = l$ and $D_{m,Rx} = 0 \, \forall n \neq l$. In this RF-coupled case, the received symbols in (8) become

$$D_{m,Rx} = d_{mn} e^{-j2\pi n\Delta f\frac{2R}{c_0}} e^{-j2\pi f_c\frac{2R}{c_0}} e^{-j2\pi f_c\frac{2v}{c_0}\frac{mN}{f_s}}. \tag{9}$$

Note that (9) is already simplified, i.e. effects such as intercarrier interference (ICI), range-Doppler migration (MIG), fast-time compression (FTC) are neglected here but discussed in detail in subsequent sections.

Finally, the transmitted symbols are removed via spectral division, leading to the spectrogram

$$D_{mn} = D_{Rx} \odot (D_{Tx})^*$$
$$= e^{-j2\pi n\Delta f\frac{2R}{c_0}} e^{-j2\pi f_c\frac{2R}{c_0}} e^{-j2\pi f_c\frac{2v}{c_0}\frac{mN}{f_s}}, \tag{10}$$

were $\odot$ is the Hadamard product and $(\cdot)^*$ the complex conjugate. Under the influence of e.g. an SFO, $D_{mn} \in \mathbb{C}^{N \times M}$ can not easily be described mathematically, since the cancellation of IDFT and DFT in (8) is not possible, resulting in a residual error. Therefore, multiple criteria are needed in order to keep this residual error negligible, which are derived in Sections IV–VI.

D. RANGE-DOPPLER ESTIMATION

The standard range-Doppler processing is based on discrete Fourier transforms. In this section, only the RF-coupled case is discussed while Sections IV–VI extend the formulas for specific coupling induced errors.
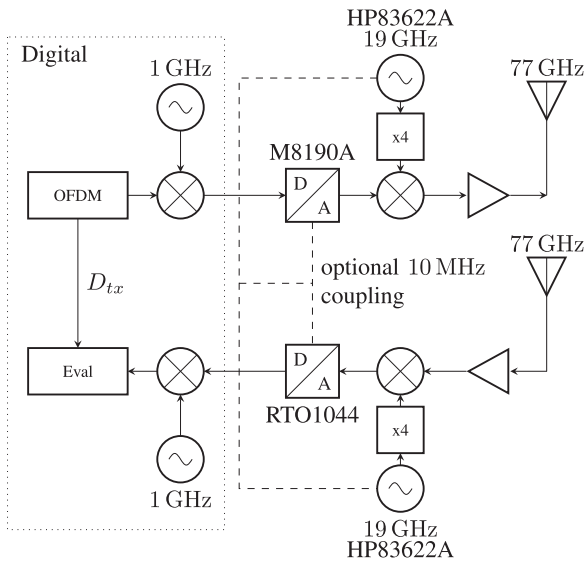
First, the target range is estimated by a column-wise IDFTs of D_{mn}, i.e. the frequency dimension, which results in the range profile

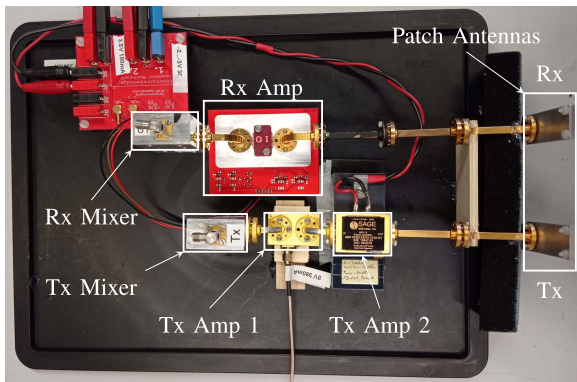$$r_m[\rho] = \sum_{n=0}^{N-1} D_{mn} e^{j2\pi\frac{n\rho}{N}}. \tag{11}$$

For every target, a maximum of the range profile can be found at index

$$\rho = \left\lfloor \frac{2R\Delta fN}{c_0} \right\rfloor. \tag{12}$$

Second, the target velocity is evaluated using a row-wise DFT of D_{mn}, i.e. the slow-time dimension, which gives the

FIGURE 1. Block diagram of the OFDM radar network measurement setup with optional 10 MHz coupling.

FIGURE 2. Photograph of the RF part of the radar demonstrator.

Doppler profile

$$v_n[\nu] = \sum_{m=0}^{M-1} D_{mn}e^{-j2\pi \frac{m\nu}{M}}. \tag{13}$$

For every target, a maximum of the Doppler profile can be found at index

$$\nu = \left\lfloor \frac{2\nu f_c TM}{c_0} \right\rfloor. \tag{14}$$

III. MEASUREMENT SETUP

To demonstrate the effects of synchronization errors and to validate the criteria derived in this paper, a 77 GHz radar demonstrator is used. Fig. 1 shows a complete block diagram of the demonstrator. A photograph of the RF part is shown in Fig. 2. It consists of one transmitter and one receiver, each built from discrete waveguide components. Separate measurement devices are used for LO generation at Tx and Rx, as well as for signal generation and sampling. This allows to flexibly run them uncoupled or LF-coupled, as well as to introduce

TABLE 1. OFDM-Radar Parameters

Parameter	Value
Bandwidth B	1 GHz
Subcarrier Spacing Δf	500 kHz
Number of Subcarriers N	2000
Number of Symbols M	1024
Cyclic Prefix Samples N_{CP}	500

specific synchronization errors. This way, the measurement setup enables a detailed analysis of the effects caused by SFO, CFO, STO, and phase noise.

On the Tx side, the OFDM signal is digitally up-converted to a 1 GHz intermediate frequency (IF) carrier before being converted to the analog domain using a Keysight M8190A arbitrary waveform generator (AWG) at a sample frequency of $f_{s,Tx} = 10$ GHz. The up-conversion to 77 GHz is realised using a subharmonic double-sideband (DSB) mixer and an HP83622A signal generator as LO, followed by two waveguide amplifiers and a patch antenna.

The RF-part of the receiver also consists of a patch antenna and two waveguide amplifiers. This is followed by a down-conversion using another DSB mixer and HP83622 A signal generator. The signal then is digitized using a R&S RTO1044 oscilloscope with $f_{s,Rx} = 10$ GHz.

All measurements and calculations are performed using the same OFDM parameters given in Table 1. Additionally, a systematic time delay caused by the measurement setup is present. This offset is taken into account if a range axis is shown, calibrating the axis and therefore also showing negative ranges.

IV. SAMPLING FREQUENCY OFFSET

An SFO occurs if the clocks of a transmitter's DAC and receiver's ADC do not match. Here, the clocks are derived from oscillators with frequencies $f_s = f_{s,Tx} \neq f_{s,Rx} = \delta_s f_s$ and always count $N = T f_s$ samples to create a single OFDM symbol of duration T. Since these counters use oscillators with different frequencies, the signal durations vary for a fixed number of samples. In case of $\delta_s < 1$, the ADCs timings are always too late and the recorded symbol duration is longer with respect to the original duration $T = \frac{N}{f_s}$. From the perspective of the transmitting radar, the timing of the opposing oscillator is always too early. As described in [18], the relative time difference $\Delta T = T - \frac{N}{\delta_s f_s}$ increases as time progresses. Therefore, with the progression of the radar frame, the timing difference is accumulated, leading to more severe errors for longer radar frames.

Without loss of generality, the sampling frequency is assumed to be the modulation bandwidth $f_s = B$. In this section, influences of other network errors are disregarded to get a better understanding of the effects caused by an SFO. Hence, no CFO or STO is present and $\delta_c = 1$. In this case, (8) can be

rewritten as

$$D_{m,\text{Rx}} = \frac{1}{N} \sum_{k=0}^{N-1} \left[\sum_{n=0}^{N-1} d_{mn} \underbrace{e^{j2\pi \frac{nk}{\delta_s N}}}_{(i,\text{IDFT})} \underbrace{e^{j2\pi \frac{nm}{\delta_s}}}_{(ii,\text{IDFT})} \underbrace{e^{-j2\pi n\Delta f \frac{2R}{c_0}}}_{(iii,R)} \right.$$

$$\times \underbrace{e^{-j2\pi f_c \frac{2R}{c_0}}}_{(iv,\text{const.})} \underbrace{e^{-j2\pi \frac{2v}{c_0} \frac{nk}{\delta_s N}}}_{(v,\text{FTC})} \underbrace{e^{-j2\pi \frac{2v}{c_0} \frac{kf_c}{\delta_s B}}}_{(vi,\text{ICI})}$$

$$\times \underbrace{e^{-j2\pi \frac{2v}{c_0} \frac{nm}{\delta_s}}}_{(vii,\text{MIG})} \left. \underbrace{e^{-j2\pi \frac{2v}{c_0} \frac{mNf_c}{\delta_s B}}}_{(viii,v)} \right]$$

$$\times \underbrace{e^{-j2\pi \frac{lk}{N}}}_{(ix,\text{DFT})} \underbrace{e^{-j2\pi lm}}_{(x,\text{DFT})}. \tag{15}$$

The exponents of terms (iii, R) and $(iv, \text{const.})$ are proportional to R and are not affected by an SFO. While (iii, R) is used for range estimation, $(iv, \text{const.})$ is constant for all n, m, k and is exploited for DoA estimation. The terms (v, FTC), (vi, ICI) and (vii, MIG) are well known in literature [21], they therefore are only briefly discussed here: (v, FTC) causes a compression/stretching in fast-time due to the targets movement and can usually be neglected since the signal is narrowband compared to its RF frequency, i.e. $f_c \gg B$ (narrowband assumption); (vi, ICI) causes a shift of OFDM subcarriers due to a targets Doppler, which leads to a reduction of orthogonality. (vi, ICI) is negligible if the motion induced Doppler is small in comparison to the subcarrier distance, i.e. $f_D \ll \Delta f$; (vii, MIG) is omitted if the change in target range within a frame due to its motion is insignificant, i.e. $vMT < \Delta R$. Otherwise, it causes a migration of the estimated range along slow-time dimension. This effect is more severe for a larger time-bandwidth product (TBP); The phase of term $(viii, v)$ is proportional to v along the slow-time dimension m and used for Doppler estimation, which is discussed in Section IV-C. The remaining terms (i, IDFT), (ii, IDFT), (ix, DFT) and (x, DFT) are the IDFT and DFT respectively. As explained in Section II-C, these terms only cancel out if $\delta_s = 1$ but result in a residual error otherwise.

To visualize the effect of an SFO, measurements of a (CR) at $R = 4.9$m and a 10 MHz coupled setup are performed. The result without an SFO is shown in Fig. 3, while the result with $f_{\text{SFO}} = 1$ MHz is displayed in Fig. 4. In Fig. 4(b) a clear distortion of the Rv image can be observed, which renders any further signal processing futile. A peak appears smeared in both directions and, in this case, with a velocity offset. As shown in Fig. 4(a), which is obtained via range evaluation as shown in (11), the spread in range direction is caused by the MIG effect of the SFO, which corresponds to (ii, IDFT) and (x, DFT). Fig. 4(c) visualizes the FTC effect caused by f_{SFO} and is obtained via velocity evaluation of the received symbols. The linear phase progression in fast-time dimension corresponds with (i, IDFT) and (ix, DFT). Also, since in this case the first subcarrier is at 1 GHz, the target peak is offset in velocity direction.
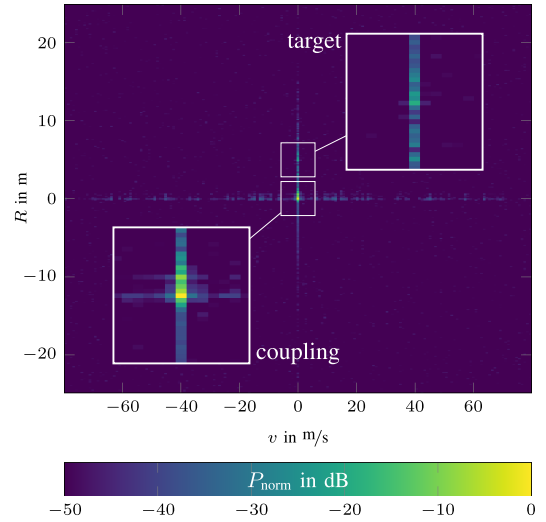

FIGURE 3. Measurement of a corner reflector (CR) at $R = 4.9$ m with a 10 MHz coupled setup and no errors. The target and direct coupling are marked.
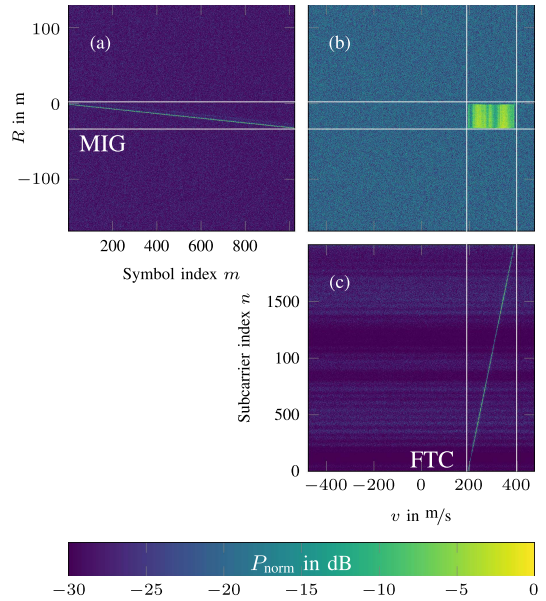

FIGURE 4. Measurement of a CR at $R = 4.9$ m with a 10 MHz coupled setup and an SFO with $f_{\text{SFO}} = 1$ MHz. (a) shows the profile after range evaluation, (b) the Rv plot, and (c) the profile after velocity evaluation.

In the following, criteria are formulated that, if met, keep this residual error small enough to be neglected. For this, similarities between the phase terms in (15) are exploited. Namely, the FTC and MIG caused by the targets movement, which are compared to the IDFT and DFT terms.

A. FIRST SFO CRITERION (FTC)
First, the phase terms of (i, IDFT) and (ix, DFT) in (15) are combined into

$$\Phi_{\text{SFO,FTC}} = 2\pi \left(\frac{n}{\delta_s} - l \right) \frac{k}{N}, \tag{16}$$
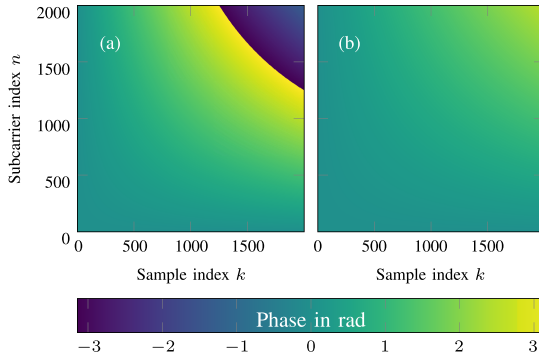
FIGURE 5. Simulation of the residual phase after multiplication of (i, IDFT) and (ix, DFT) (see equation (15)). In (a) for $\delta_s = \delta_{SFO,FTC}$ and (b) for $\delta_{SFO,FTC} < \delta_s < 1$.

FIGURE 6. Simulation of the residual phase after multiplication of (ii, IDFT) and (x, DFT) (see equation (15)). In (a) for $\delta_s = \delta_{SFO,MIG}$ and (b) for $\delta_{SFO,MIG} < \delta_s < 1$.

with the discrete frequencies n and l. Without an SFO, $\Phi_{SFO,FTC} = 0$ for $n = l$ and $e^{j\Phi_{SFO,FTC}} = 0$ for $n \neq l$, resulting in the standard OFDM signal demodulation explained in Section II-C. With an SFO, a compression or scaling of the signal along fast-time dimension occurs, similar to (v, FTC). In [22], a criterion for the FTC has already been formulated. It describes that the amount of compression or scaling that the OFDM symbol is allowed to experience should be less than the critical sampling period and according to the Nyquist sampling criterion, yields
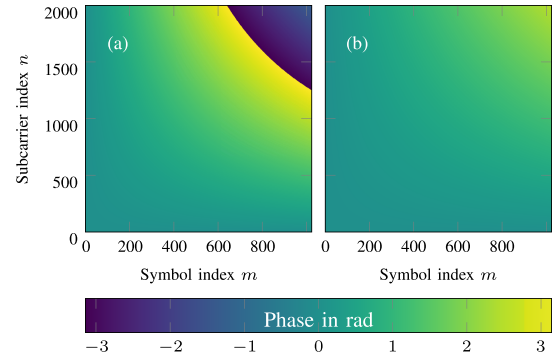
$$T\frac{2v}{c_0} < \frac{1}{N\Delta f} \Longleftrightarrow \frac{2v}{c_0} < \frac{1}{BT}. \qquad (17)$$

For (v, FTC), the scaling factor and cause of the effect is $\frac{2v}{c_0}$. In case of the FTC observed in $\Phi_{SFO,FTC}$ the term $\frac{2v}{c_0}$ is substituted with $(\frac{1}{\delta_s} - 1)$. This assumption is valid for $n = l$, which is true since $\Phi_{SFO,FTC} = 0$, $\forall n \neq l$. Solving for δ_s yields

$$\left(\frac{1}{\delta_s} - 1\right) < \frac{1}{BT}$$

$$\Longleftrightarrow \delta_s > \frac{1}{1 + \frac{1}{BT}} := \delta_{SFO,FTC}, \qquad (18)$$

which is referred to as the first SFO criterion in the following. As the TBP gets larger, $\delta_{SFO,FTC}$ approaches one ($\delta_{SFO,FTC} \xrightarrow{BT \gg 1} 1$) and therefore the required precision of the sampling rate increases.

A visualization of this criterion is shown in Fig. 5. The two figures show the phase of the residual error $\Phi_{SFO,FTC}$ for all possible k and n. For this, the parameters in Table 1 are used. In the error-free case, the phase progression is a plane, i.e. no change in phase over k and n. In Fig. 5(a) $\delta_s = \delta_{SFO,FTC} \approx 0.9996$, i.e. the critical case, a phase offset of 2π is present resulting in a slight compression in fast-time. Fig. 5(b) is calculated using $\delta_s = \delta_{SFO,FTC} + 0.0002$, which satisfies the criterion and reduces the residual phase shift to a tolerable level.

B. SECOND SFO CRITERION (MIG)

Finally, the remaining phase terms (ii, IDFT) and (x, DFT) are combined into

$$\Phi_{SFO,MIG} = 2\pi \left(\frac{n}{\delta_s} - l\right) m. \qquad (19)$$

Without an SFO, i.e. $\delta_s = 1$, $\Phi_{SFO,MIG}$ will always be an integer multiple of 2π and therefore $e^{j\Phi_{SFO,MIG}} \stackrel{\delta_s=1}{=} 1$. With an SFO, an error similar to (vii, MIG) is observed, leading to a change in target range along slow-time dimension due to the targets Doppler. As mentioned in Section IV, this change should be less than the range resolution ΔR, leading to [23]

$$vMT < \Delta R \Longleftrightarrow \frac{2v}{c_0} < \frac{2\Delta R}{c_0 MT} = \frac{1}{MBT}. \qquad (20)$$

If this criterion for the targets movement is met, the migration along slow-time dimension is less then one range bin. Again, the scaling factor $\frac{2v}{c_0}$ of (vii, MIG) is substituted with $(\frac{1}{\delta_s} - 1)$, which is the scaling factor observed in $\Phi_{SFO,MIG}$. Solving for δ_s yields

$$\left(\frac{1}{\delta_s} - 1\right) < \frac{1}{MBT}$$

$$\Longleftrightarrow \delta_s > \frac{1}{1 + \frac{1}{MBT}} := \delta_{SFO,MIG}. \qquad (21)$$

Formula (21) is referred to as the second SFO criterion. Similarly to (18), (21) also scales with the TBP ($\delta_{SFO,MIG} \xrightarrow{BT \gg 1} 1$), which is additionally multiplied with the number of OFDM symbols per frame. Therefore, a higher number of transmitted OFDM symbols leads to a stricter SFO requirement ($\delta_{SFO,MIG} \xrightarrow{M \gg 1} 1$), since the change in target range occurs for a longer observation time. As noted before, the relative time difference ΔT between two uncoupled clocks also increases with longer radar frames, leading to a stricter criterion for effects across slow-time dimension.

Again, the phase of the residual error $\Phi_{SFO,MIG}$ in Fig. 6 is calculated for all possible subcarriers n, slow-time counts m. All modulation parameters used can be found in Table 1. Fig. 6(a) shows the residual phase at

$\delta_s = \delta_{SFO,MIG} \approx 0.9999996$, while Fig. 6(b) uses $\delta_s = \delta_{SFO,MIG} + 0.0000002$ and satisfies the criterion. When comparing the values of $\delta_{SFO,MIG}$ and $\delta_{SFO,FTC}$ it is obvious that the former requires a much stricter synchronization due to the scaling with observation time.

If the first and second criteria are met, i.e. $1 \geq \delta_s \gg \delta_{SFO,FTC}$ and $1 \geq \delta_s \gg \delta_{SFO,MIG}$, the IDFT and DFT in (15) can be calculated with no or minimal residual error and the received symbols become

$$D_{m,Rx} = d_{mn} e^{-j2\pi n \Delta f \frac{2R}{c_0}} e^{-j2\pi f_c \frac{2R}{c_0}} e^{-j2\pi \frac{2v}{c_0} \frac{mN f_c}{\delta_s B}}. \qquad (22)$$

Compared to the received symbols in (9), the Doppler term is shifted by $\frac{1}{\delta_s}$, leading to an error in estimated velocity. An analytical solution is derived in Section IV-C. Finally, the spectral division can be performed as described by (10), resulting in the demodulated spectrogram

$$D_{mn} = e^{-j2\pi n \Delta f \frac{2R}{c_0}} e^{-j2\pi f_c \frac{2R}{c_0}} e^{-j2\pi \frac{2v}{c_0} \frac{mN f_c}{\delta_s B}}, \qquad (23)$$

which is used for range-Doppler evaluation. It should be noted that the error in estimated velocity, caused by the factor δ_s, is already small, since the aforementioned criteria have to be met in order to reach this point.

C. THIRD SFO CRITERION (DOPPLER)

Since (23) only differs from (10) in its Doppler term, the range estimation is identical to the one described in Section II-D and therefore skipped, and only the Doppler estimation via DFT along slow-time dimension is considered. In the presence of an SFO, the Doppler estimation yields

$$v_n[\nu] = e^{-j2\pi n \Delta f \frac{2R}{c_0}} e^{-j2\pi f_c \frac{2R}{c_0}}$$
$$\times \sum_{m=0}^{M-1} \left[e^{-j2\pi \frac{2v}{c_0} \frac{mN f_c}{\delta_s B}} \right] e^{-j2\pi \frac{mv}{M}}. \qquad (24)$$

A maximum of (24) then occurs at bin

$$v_{SFO} = \left\lfloor \frac{1}{\delta_s} \cdot \frac{2v f_c T M}{c_0} \right\rfloor, \qquad (25)$$

which only differs from the standard OFDM processing by a factor of $\frac{1}{\delta_s}$. Since the aforementioned criteria are already in place, this offset is close to zero and therefore negligible.

For completeness sake, a third criterion can be formulated by limiting (25) to a maximum error of one bin, which results in

$$\delta_s > \frac{1}{1 + \frac{2}{M}} := \delta_{SFO,v}, \qquad (26)$$

where $\pm \frac{M}{2}$ is the maximum possible velocity bin offset.

D. MEASUREMENTS USING THE CRITERIA

To validate the three SFO criteria, again measurements of a CR at range $R = 4.9$ m are analysed. First the critical SFO values of the three criteria are calculated using the parameters from Table 1. The results are given in Table 2. Since $1 \geq \delta_{SFO,MIG} > \delta_{SFO,FTC} > \delta_{SFO,v}$ is always true, only

TABLE 2. Critical SFO Values

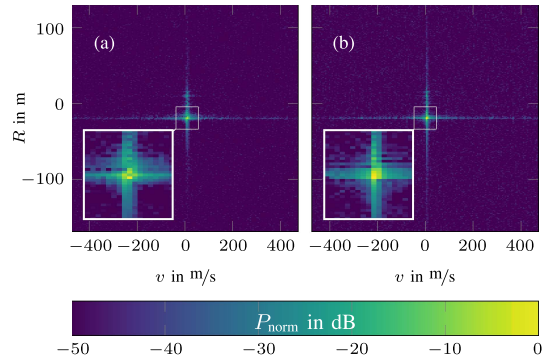| Parameter	Value
$f_{SFO}(\delta_{SFO,FTC})$	4.875 MHz
$f_{SFO}(\delta_{SFO,MIG})$	4.736 kHz
$f_{SFO}(\delta_{SFO,v})$	19.493 MHz

FIGURE 7. Measurements of a CR at $R = 4.9$ m and a 10 MHz coupled setup. R_v evaluation was performed on the received symbols. In (a) with $f_{SFO} = 6$ kHz, therefore slightly over the suggested $f_{SFO}(\delta_{SFO,FTC})$. (b) with $f_{SFO} = 4$ kHz, which meets $f_{SFO}(\delta_{SFO,MIG})$.

$\delta_{SFO,MIG}$ is needed to achieve sufficient synchronization. To isolate the effects caused by an SFO from other coupling induced errors, a 10 MHz coupled network architecture is used. An SFO is artificially introduced by altering the sampling rate of the AWG. Fig. 7(a) shows the Range-Doppler map for $f_{SFO} = 6$ kHz, which violates $f_{SFO}(\delta_{SFO,MIG}) = 4.736$ kHz. Compared to Fig. 7(b), which meets $f_{SFO} = 4$ kHz $< f_{SFO}(\delta_{SFO,MIG})$, the peak is slightly more smeared, since the migration over the symbol index m exceeds one bin. To summarize, while the first criterion limits the FTC effect caused by an SFO, the MIG effect is much more severe since it additionally scales with the number of transmitted symbols. When $\delta_{SFO,MIG}$ is just met, the migration in slow-time direction can reach a maximum of one bin. For high precision applications, the level of synchronization needed might be even higher, in which case δ_s should be well above the critical value, i.e. $1 \geq \delta_s \gg \delta_{SFO,MIG}$.

V. CARRIER FREQUENCY OFFSET

In case of a CFO, there is a mismatch of the carrier frequencies $f_{c,Tx} \neq f_{c,Rx}$ for up- and downconversion of the OFDM signal, that results in a residual carrier frequency offset $f_{CFO} = f_{c,Rx} - f_{c,Tx}$. This shift is similar to a Doppler frequency shift, including all errors which originate from a Doppler frequency shift, e.g. ICI. If both $f_{c,Tx}$ and $f_{c,Rx}$ are derived from the same REF, both frequencies are equal and $f_{CFO} = 0$ Hz.

Without loss of generality, the following derivation assumes an ideal Tx LO with $f_{c,Tx} = f_c$ and an Rx LO with $f_{c,Rx} = \delta_c f_c$. In that case, the CFO is $f_{CFO} = (1 - \delta_c) f_c$. To separate the effect of a CFO from other network related errors, the sampling is assumed to be ideal, hence $f_{s,Tx} = f_{s,Rx} = f_s = B$.

Subsequently, (8) becomes

$$D_{m,\mathrm{Rx}} = \frac{1}{N} \sum_{k=0}^{N-1} \left[\sum_{n=0}^{N-1} d_{mn} \underbrace{e^{j2\pi\frac{nk}{N}}}_{(i,\mathrm{IDFT})} \underbrace{e^{j2\pi nm}}_{(ii,\mathrm{IDFT})} \underbrace{e^{-j2\pi n\Delta f\frac{2R}{c_0}}}_{(iii,R)} \right.$$

$$\times \underbrace{e^{-j2\pi f_c\frac{2R}{c_0}}}_{(iv,\mathrm{const.})} \underbrace{e^{-j2\pi\frac{2v}{c_0}\frac{nk}{N}}}_{(v,\mathrm{FTC})} \underbrace{e^{-j2\pi\frac{2v}{c_0}\frac{kf_c}{B}}}_{(vi,\mathrm{ICI})}$$

$$\times \underbrace{e^{j2\pi(1-\delta_c)\frac{kf_c}{B}}}_{(xii,\mathrm{CFO})} \underbrace{e^{-j2\pi\frac{2v}{c_0}nm}}_{(vii,\mathrm{MIG})} \underbrace{e^{-j2\pi\frac{2v}{c_0}\frac{mNf_c}{B}}}_{(viii,v)}$$

$$\times \left. \underbrace{e^{j2\pi(1-\delta_c)\frac{mNf_c}{B}}}_{(xi,\mathrm{CFO})} \right] \underbrace{e^{-j2\pi\frac{lk}{N}}}_{(ix,\mathrm{DFT})} \underbrace{e^{-j2\pi lm}}_{(x,\mathrm{DFT})}. \quad (27)$$

Most of the phase terms in (27) have already been discussed in Section IV. Again, terms (v, FTC), (vi, ICI) and (vii, MIG) can be ignored, since the targets velocity is assumed to be small enough, as specified before. (iii, R) and $(viii, v)$ are used for range Doppler estimation and are discussed in Section V-B. While (xi, CFO) must be considered for the subsequent Doppler evaluation, it has no impact on the demodulation, since the exponent is only proportional to m. Compared to (15) again, the IDFT and DFT terms do not cancel completely as (xii, CFO) introduces an ICI effect.

To visualize the effect of an CFO, measurements of a (CR) at $R = 4.9$ m and 10 MHz are performed. The results are shown in Fig. 8. Fig. 8(a) shows the Rv map of a measurement with $f_{\mathrm{CFO}} = 17$ kHz, where a significant shift of the target peak in velocity direction can be observed, which corresponds to (xi, CFO). Additionally, the ICI effect induced by (xii, CFO) causes a signal-to-noise ratio (SNR) degradation due to the reduced orthogonality of the subcarriers. A comparison to a measurement with $f_{\mathrm{CFO}} = 0$ Hz can be found in Fig. 8(b). There, the velocity profile at $R = 0$ m is displayed, which clearly shows the offset caused by the CFO.

In case of small f_{CFO}, the phases of (xi, CFO) and (xii, CFO) in (27) become negligible.

### A. FIRST CFO CRITERION (ICI)

Term (xii, CFO) is proportional to the sample index k, similar to term (vi, ICI), causing a shift of OFDM subcarriers and therefore reducing the orthogonality if it is not fully compensated for. The ICI caused by a target's Doppler is discussed in detail in [21], where a threshold of $\Delta f > 10 f_{\mathrm{D,max}}$ is proposed, for the maximum tolerable target Doppler $f_{\mathrm{D,max}}$. A similar criterion can be derived for a CFO:

$$\Delta f > 10(1 - \delta_c) f_c$$

$$\implies \delta_c > 1 - \frac{\Delta f}{10 f_c} := \delta_{\mathrm{CFO,ICI}} \xrightarrow{\Delta f \to 0} 1. \quad (28)$$

Formula (28) is referred to as the first CFO criterion. It scales inversely proportional to the subcarrier spacing Δf, since the loss of orthogonality is more severe for tightly spaced subcarriers. In Fig. 9, the phase progression of (xii, CFO)
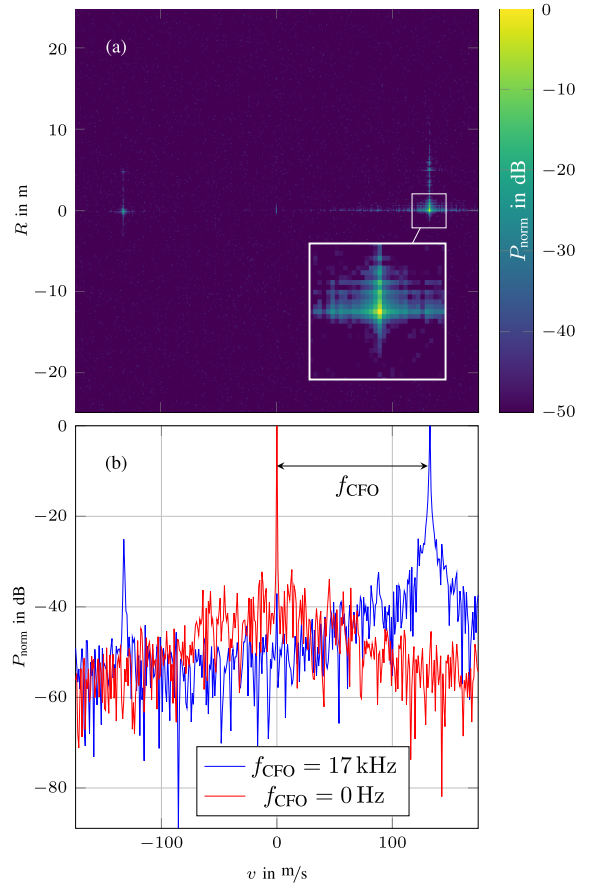
FIGURE 8. Measurement of a CR at $R = 4.9$ m and 10 MHz coupling. In (a), the cut in velocity direction at max(P_{norm}) is displayed for (blue) $f_{\mathrm{CFO}} = 0$ Hz and (red) $f_{\mathrm{CFO}} = 17$ kHz. (b) shows the corresponding cuts in range direction at max(P_{norm}).
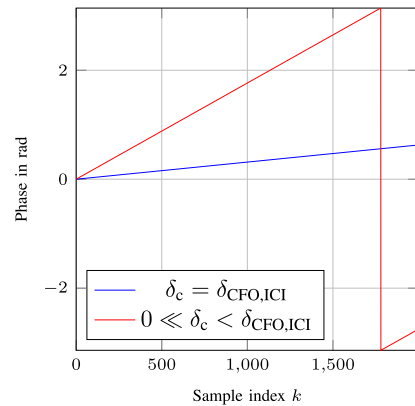
FIGURE 9. Simulation of the residual phase of (xii, CFO) for different δ_c. While $\delta_c = \delta_{\mathrm{CFO,ICI}}$ is the critical value, it already shows an almost negligible phase offset across k. For $0 \ll \delta_c < \delta_{\mathrm{CFO,ICI}}$ the phase progression becomes steeper and therefore increases the loss of orthogonality.

along the sample index k is visualized for two different δ_c. For this, the modulation parameters in Table 1 are used. First, the phase for the critical value $\delta_c = \delta_{\mathrm{CFO,ICI}} \approx 0.9999993$ is calculated and only causes an overall phase shift of $\approx 0.2\pi$, while $\delta_c = \delta_{\mathrm{CFO,ICI}} - 0.000003$, which fails to meet the

criterion, causes an overall phase shift of 2π. Since the SNR degrades with increasing phase shift due to (*xii*, CFO), the first CFO criterion ensures this phase progression is small enough to be negligible.

If (28) is met, i.e. $1 \geq \delta_c \gg \delta_{\text{CFO,ICI}}$, the IDFT and DFT can be calculated with no residual error and (27) can be written as

$$D_{m,\text{Rx}} \approx d_{mn} \mathrm{e}^{-j2\pi n \Delta f \frac{2R}{c_0}} \mathrm{e}^{-j2\pi f_c \frac{2R}{c_0}} \mathrm{e}^{-j2\pi \frac{2v}{c_0} \frac{mNf_c}{B}}$$
$$\times \mathrm{e}^{j2\pi(1-\delta_c)\frac{mNf_c}{B}}. \tag{29}$$

After spectral division as described in (10), the demodulated spectrogram is given by

$$D_{mn} = \mathrm{e}^{-j2\pi n \Delta f \frac{2R}{c_0}} \mathrm{e}^{-j2\pi f_c \frac{2R}{c_0}} \mathrm{e}^{j2\pi(1-\delta_c-\frac{2v}{c_0})\frac{mNf_c}{B}}. \tag{30}$$

Note that there is still a remaining error in velocity direction when compared to (10), which is further investigated in the following section.

B. SECOND CFO CRITERION (DOPPLER)

Using the spectrogram from (30), the range and velocity can be estimated as described in Section II-D. Since the terms proportional to R are not affected by a CFO, only the velocity estimation is considered in this Section. With (30) the Doppler DFT (13) gives

$$v_n[v] = \mathrm{e}^{-j2\pi n \Delta f \frac{2R}{c_0}} \mathrm{e}^{-j2\pi f_c \frac{2R}{c_0}} \sum_{m=0}^{M-1} \left[\mathrm{e}^{j2\pi(1-\delta_c-\frac{2v}{c_0})\frac{mNf_c}{B}} \right]$$
$$\times \mathrm{e}^{-j2\pi \frac{mv}{M}}. \tag{31}$$

A maximum of (31) can be found at

$$v_{\text{CFO}} = \left\lfloor \frac{2v f_c T M}{c_0} \pm (1 - \delta_c) f_c T M \right\rfloor, \tag{32}$$

which differs from the ideal velocity estimate (14) by $\pm(1-\delta_c)f_c T M$. Thus, a second criterion can be found by limiting this shift in velocity to one bin, which can be written as

$$|(1 - \delta_c) f_c T M| < 1$$
$$\Longleftrightarrow \delta_c > 1 - \frac{1}{f_c T M} := \delta_{\text{CFO,v}}. \tag{33}$$

However, this criterion is very harsh, since it inversely scales with the carrier frequency and observation time. Alternatively, if an error estimation and correction in post processing is applied, the shift in velocity can also be limited to the maximum unambiguous velocity v_{ua} while considering the maximum expected target velocity v_{max}. The relaxed alternative criterion can formulated as

$$\frac{c_0}{2\cancel{f_c}} (1 - \delta_c) \cancel{f_c} < v_{\text{ua}} - v_{\text{max}}$$
$$\Longleftrightarrow \delta_c > 1 - \frac{2(v_{\text{ua}} - v_{\text{max}})}{c_0} := \delta_{\text{CFO,v,Alt}}. \tag{34}$$

If this criterion is met, i.e. $1 \geq \delta_c > \delta_{\text{CFO,v,Alt}}$, a shift in velocity may occur but can be corrected without any ambiguities.

TABLE 3. Critical CFO Values

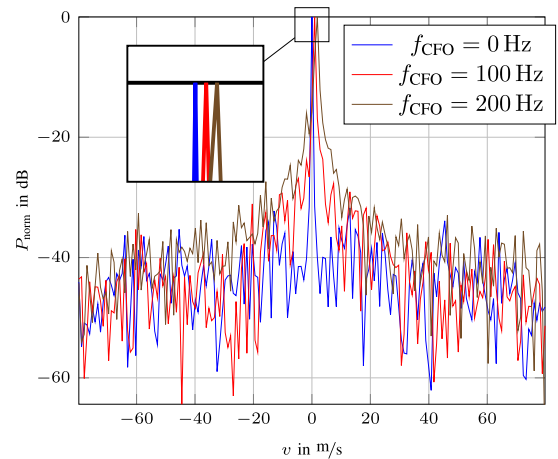| Parameter	Value
$f_{\text{CFO}}(\delta_{\text{CFO,ICI}})$	12.337 kHz
$f_{\text{CFO}}(\delta_{\text{CFO,v}})$	117.546 Hz
$f_{\text{CFO}}(\delta_{\text{CFO,v,Alt}})$	54.165 kHz

FIGURE 10. Measurement of a CR at $R = 4.9$ m and 10 MHz coupling. Displayed is the cut in velocity direction and at $R(\max(P_{\text{norm}}))$ for (red) $f_{\text{CFO}} = 100$ Hz and (blue) $f_{\text{CFO}} = 200$ Hz.

C. MEASUREMENTS USING THE CRITERIA

Finally, measurements of a CR at $R = 4.9$ m with 10 MHz coupling are performed for different $f_{\text{CFO}}(\delta_c)$. The LF-coupled architecture is chosen to negate any inherent frequency offsets. Furthermore, by adjusting the LO frequency on the receiver side, a CFO can be introduced artificially. The derived CFO criteria are calculated using the modulation parameters in Table 1 and are shown in Table 3. Again, only the harshest criteria $\delta_{\text{CFO,v}}$ needs to be met for sufficient synchronization. As shown in Fig. 10, a CFO of $f_{\text{CFO}} = 100$ Hz (red) meets the criterion $f_{\text{CFO}}(\delta_{\text{CFO,v}}) = 117.546$ Hz with a velocity offset of maximum one bin, while $f_{\text{CFO}} = 200$ Hz (blue) shifts the detected peak to the second bin. To summarize, the first CFO criterion only ensures minimal SNR loss, while the second and third CFO criteria limit the shift in velocity direction. If this shift is corrected with the methods in Section VIII, a more lenient synchronization is possible.

VI. SYMBOL TIMING OFFSET

If the frame start time t_0 of the transmitting and receiving sensors misalign, i.e. $t_{0,\text{Tx}} = t_0 \neq t_{0,\text{Rx}} = t_0 + \Delta t_0$, a STO occurs. This is modelled by adding an additional time delay Δt_0 to (4), which can be written as

$$y_m^{\text{RF}}(t) = x_m^{\text{RF}}(t - \tau(t) - \Delta t_0). \tag{35}$$

From (35) it is apparent that an STO has an effect similar to that of the time-of-flight $\tau(t)$.

To isolate the STO from other network specific errors, the sampling and carrier frequencies are assumed to be ideal, i.e.

$f_{s,Tx} = f_{s,Rx} = f_s = B$ and $f_{c,Tx} = f_{c,Rx} = f_c$, with the modulation bandwidth B as sample rate. In that case, (8) becomes

$$D_{m,Rx} = \frac{1}{N} \sum_{k=0}^{N-1} \left[\sum_{n=0}^{N-1} d_{mn} \underbrace{e^{j2\pi \frac{nk}{N}}}_{(i,IDFT)} \underbrace{e^{j2\pi nm}}_{(ii,IDFT)} \underbrace{e^{-j2\pi n\Delta f \frac{2R}{c_0}}}_{(iii,R)} \right.$$

$$\times \underbrace{e^{-j2\pi f_c \frac{2R}{c_0}}}_{(iv,const.)} \underbrace{e^{-j2\pi n\Delta f \Delta t_0}}_{(xiii,STO)} \underbrace{e^{-j2\pi f_c \Delta t_0}}_{(xiv,STO)}$$

$$\times \underbrace{e^{-j2\pi \frac{2v}{c_0} \frac{nk}{N}}}_{(v,FTC)} \underbrace{e^{-j2\pi \frac{2v}{c_0} \frac{kf_c}{B}}}_{(vi,ICI)} \underbrace{e^{-j2\pi \frac{2v}{c_0} nm}}_{(vii,MIG)}$$

$$\times \left. \underbrace{e^{-j2\pi \frac{2v}{c_0} \frac{mNf_c}{B}}}_{(viii,v)} \right] \underbrace{e^{-j2\pi \frac{lk}{N}}}_{(ix,DFT)} \underbrace{e^{-j2\pi lm}}_{(x,DFT)} \quad (36)$$

$$= d_{mn} e^{-j2\pi n\Delta f \frac{2R}{c_0}} e^{-j2\pi f_c \frac{2R}{c_0}} e^{-j2\pi \frac{2v}{c_0} \frac{mNf_c}{B}}$$

$$\times e^{-j2\pi n\Delta f \Delta t_0} e^{-j2\pi f_c \Delta t_0}. \quad (37)$$

Compared to (8), two additional terms $(xiii, STO)$ and (xiv, STO) emerge due to STO. However, they do not depend on the subcarrier index n or symbol index m. Again, the targets velocity is assumed to be sufficiently small, thus terms (v, FTC), (vi, ICI) and (vii, MIG) are negligible. Therefore, (36) reduces to (37).

The demodulated spectrogram is again obtained via spectral division of (37) with the transmitted symbols and yields

$$D_{mn} = e^{-j2\pi n\Delta f\left(\frac{2R}{c_0}+\Delta t_0\right)} e^{-j2\pi f_c\left(\frac{2R}{c_0}+\Delta t_0\right)} e^{-j2\pi \frac{2v}{c_0} \frac{mNf_c}{B}}. \quad (38)$$

Even though the presence of an STO does not affect the demodulation, the following range estimation is erroneous due to the additional time delay Δt_0.

To visualize the impact of an STO on the radar image, measurements of a CR at $R = 4.9$ m are performed using an LF coupled network with coupled 10 MHz reference. The LF-coupling mitigates potential frequency offsets, e.g. SFO, CFO. An STO is induced artificially by shifting the AWG's trigger signal. In Fig. 11(a), the Rv plot for a shift of $\Delta t_0 = 500$ ns is shown. The influence of $(xiii, STO)$ is clearly visible as the range of the detected peaks is shifted in positive range direction. Other effects are not visible, which coincides with the findings above. For comparison, Fig. 11(b) shows the range profile at the target velocity for $\Delta t_0 = 0$ s (red) and $\Delta t_0 = 500$ ns (blue). The diminished SNR is caused by the ISI effect of the delayed symbols. Usually, a sufficiently long CP prevents this SNR degradation as explained in [20].

To limit the range offset and SNR loss due to STO, a criterion is formulated in the following section.

A. STO CRITERION (RANGE)

Using the spectrogram (38), the range and velocity can be estimated. Since only the terms proportional to R are affected by the STO, the velocity estimation is omitted in the following. The target range is determined via the IDFT (13) along the
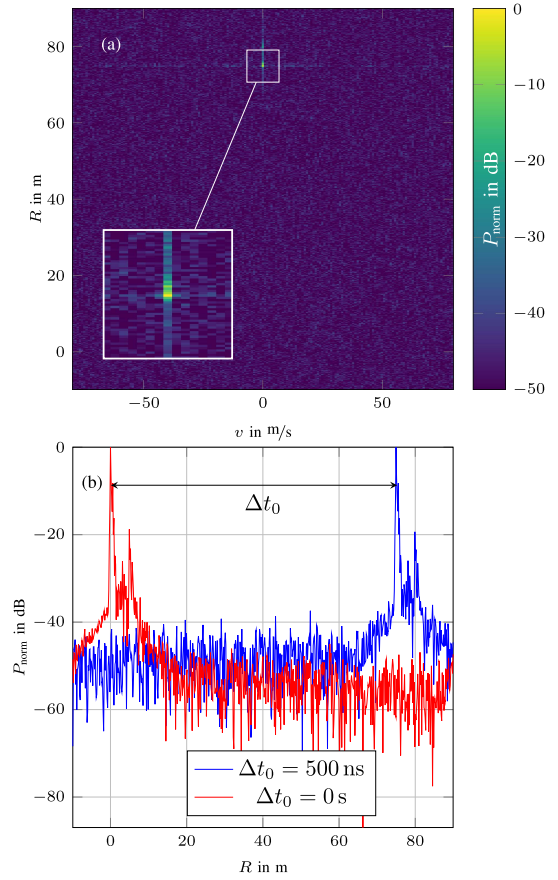
FIGURE 11. Measurement of a CR at $R = 4.9$ m and 10 MHz coupling. In (a) the range-Doppler map is displayed and (b) shows the cut in range direction at $v(\max(P_{norm}))$ for (red) $\Delta t_0 = 0$ s and (blue) $\Delta t_0 = 500$ ns.

subcarriers n and yields

$$r_m[\rho] = e^{-j2\pi f_c\left(\frac{2R}{c_0}+\Delta t_0\right)} e^{-j2\pi \frac{2v}{c_0} \frac{mNf_c}{B}}$$

$$\times \sum_{n=0}^{N-1} \left[e^{-j2\pi n\Delta f\left(\frac{2R}{c_0}+\Delta t_0\right)} \right] e^{j2\pi \frac{n\rho}{N}}. \quad (39)$$

A maximum of (39) can be found at

$$\rho_{STO} = \left\lfloor \frac{2R\Delta fN}{c_0} + \Delta f \Delta t_0 N \right\rfloor, \quad (40)$$

which only differs from the coherent maximum by $\Delta f \Delta t_0 N$.

To keep this range estimation error within one bin, the following criterion must be met:

$$\Delta f \Delta t_0 N < 1$$

$$\iff \Delta t_0 < \frac{1}{B} := T_{STO,R}. \quad (41)$$

Hence, the maximum allowed offset $T_{STO,R}$ corresponds to the Nyquist sampling interval $\frac{1}{B}$. Alternatively, if an error estimation and correction in post processing is applied, the range estimation error can also be limited to the maximum channel length R_{CP}, which depends on the duration T_{CP}, while considering the maximum expected target range R_{max}. In that

TABLE 4. Critical STO Values

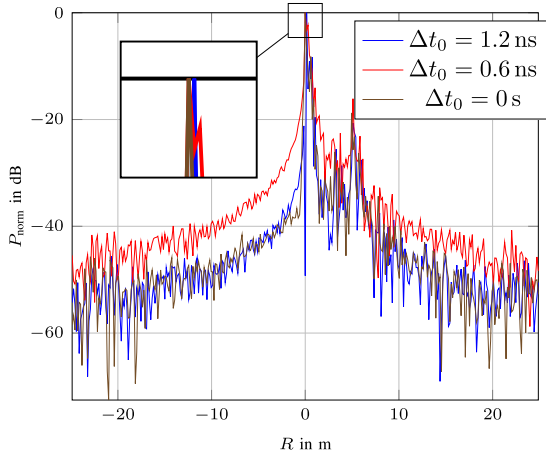| Parameter	Value
$T_{STO,R}$	1 ns
$T_{STO,R,Alt}$	975 ns

FIGURE 12. Measurement of a CR at R = 4.9 m and 10 MHz coupling. Displayed is the range profile for (blue) Δt_0 = 1.2 ns, (red) Δt_0 = 0.6 ns and (brown) Δt_0 = 0 s.

case, the relaxed criterion gives

$$\Delta t_0 c_0 < R_{CP} - R_{max}$$

$$\iff \Delta t_0 < \frac{(R_{CP} - R_{max})}{c_0} := T_{STO,R,Alt}. \qquad (42)$$

If $0 \leq \Delta t_0 < T_{STO,R,Alt}$ is met, a range offset may occur but can be corrected without any ambiguities. Note that the cyclic prefix has to be chosen accordingly, i.e. $R_{CP} > R_{max}$.

B. MEASUREMENTS USING THE CRITERION

To validate the derived criteria, measurements of a CR at R = 4.9 m with a 10 MHz coupled setup are performed. The critical STO values from (41) and (42) are displayed in Table 4. Furthermore, only the more stringent criterion is taken into consideration. An STO of Δt_0 = 1.2 ns > $T_{STO,R}$ and Δt_0 = 0.6 ns < $T_{STO,R}$ is artificially induced, which is displayed in Fig. 12. Again, the measurement is compared to Δt_0 = 0 s and only the range profiles are shown. In agreement to the derived criteria, a range offset is only visible in the case of Δt_0 = 1.2 ns. The higher skirt observed for Δt_0 = 0.6 ns is attributed to the the fact that the peak is situated between two bins.

VII. PHASE NOISE

In [24] the effects of PN on OFDM radar has been investigated for single sensors. However, for sensor networks, the impact of PN heavily depends on the network architecture and signal synthesis hardware. While RF coupled networks retain the coherency of PN, LF coupled or uncoupled architectures do not.

TABLE 5. SNR for Different Coupling Mechanisms

Coupling mechanism	SNR in dB
RF coupled	54.984
LF coupled	54.022
uncoupled	50.913

In the radar network case, there are two effects induced by uncorrelated PN. Both effects can be described as the multiplication of the complex OFDM signal $x_m^{RF}(t)$ by $e^{j\theta(t)}$. The receiver applies a DFT on the sampled signal given by

$$D_{m,Rx} = DFT\left(y_m[k]e^{j(\theta_{Tx}[k] - \theta_{Rx}[k])}\right). \qquad (43)$$

The result can be considered as the convolution in frequency domain of the received signal OFDM symbols and the phase noise spectrum. Therefore, each subcarrier is affected by the other $N-1$ subcarriers, causing ICI, resulting in SNR degradation similar to Gaussian noise. This degradation depends on the synthesizers bandwidth as well as the subcarrier spacing Δf [25].

The second effect due to uncorrelated PN introduces a skirt in Doppler domain. By mixing of the received signal with a LO, the PN degrades the phase progression in slow-time. After applying the Doppler Fast Fourier Transform (FFT), the resulting skirt at every detected target shows a velocity skirt that follows the LO PN. As explained in [19], this skirt is not only proportional to the LO's phase noise power spectral density (PSD), but also the Doppler resolution. Since a velocity skirt could potentially hinder the detection of a weaker target in the same range cell as a stronger one, it is especially relevant for automotive applications.

To illustrate the impact of PN in radar networks with different coupling mechanisms, multiple measurements are performed and shown in Fig. 13: (brown) RF coupled network using only one LO for both, transmitter and receiver path, as well as a 10 MHz coupling of the Keysight M8190A, R&S RTO1044 and HP83622A; (red) LF coupled network using two 10 MHz coupled HP83622A; (blue) uncoupled network using free-running components; For each, the range and velocity profiles are shown. In Fig. 13(a), the velocity profiles of all mentioned coupling mechanisms are shown. A clear decrease in SNR is visible, coinciding with the ICI effect caused by uncorrelated phase noise. In Table 5, the estimated SNR for all coupling mechanisms are listed. The spread in velocity direction caused by phase noise is noticeable even for the LF coupled measurement, whereas the noise power is very close to the RF coupled setup Additionally, in the uncoupled case a frequency offset, i.e. SFO and CFO, is present. Fig. 13(b) shows the range profiles, where only the decrease in SNR is noticeable.

VIII. ESTIMATION & CORRECTION

In the next step, digital error estimation and correction methods for radar networks are proposed. The concepts in this section are applicable to typical digital radar modulations, e.g.
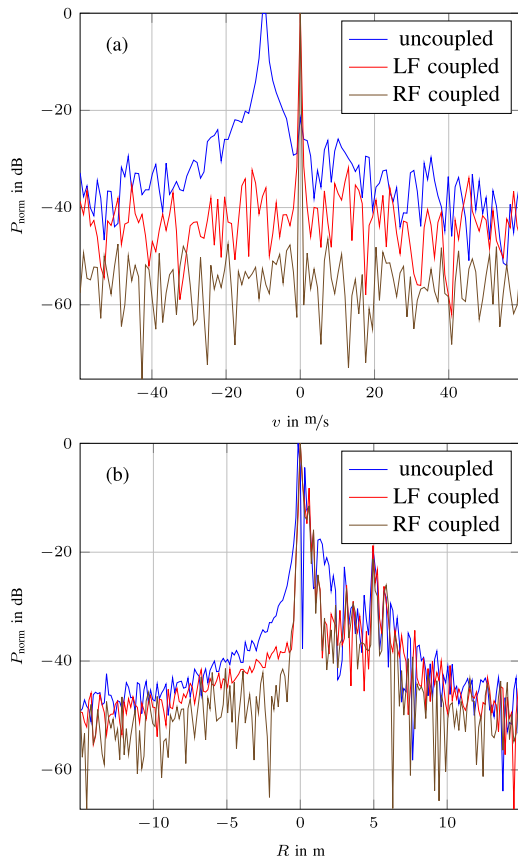
FIGURE 13. Comparison of measurements of a CR at $R = 4.9$ m for an RF (black), LF (brown) coupled and uncoupled (red) network architecture. In (a) the velocity profile is shown, while (b) displays the range profile.
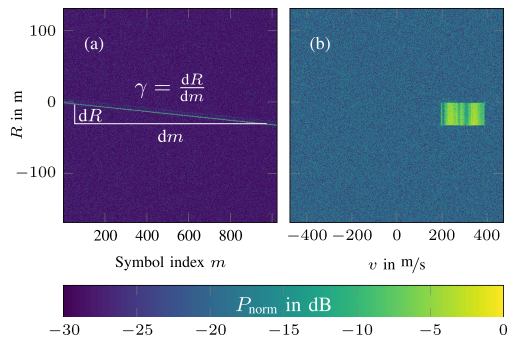

FIGURE 14. Measurement of a CR at $R = 4.9$ m, a 10 MHz coupled setup and an artificial $f_{SFO} = 1$ MHz. (a) shows the range profile and (b) the Rv plot of the measurement.

OFDM or PMCW. Their goal is to mitigate the frequency and timing offsets caused by an uncoupled network topology. This way, hardware requirements can be loosened and synchronization of time and frequency is achieved by signal processing.

A. SAMPLE FREQUENCY OFFSET

The concept of the proposed SFO error estimation method is visualized in Fig. 14. If the slope γ of the phase progression
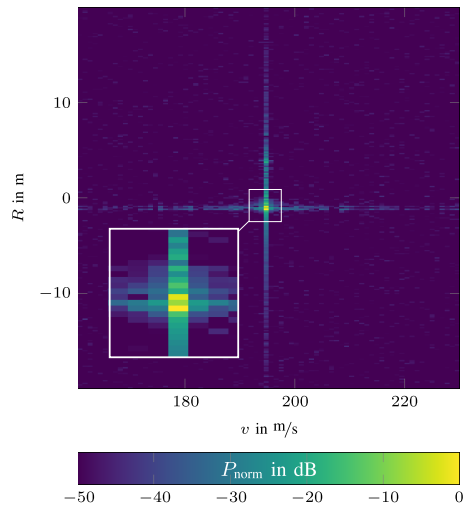
FIGURE 15. Corrected Rv plot of a measurement with $f_{SFO} = 1$ MHz. The resampling was performed using the estimated SFO $f_{SFO,est}$.

in Fig. 14(a) is known, f_{SFO} can be calculated by

$$f_{SFO} = \gamma f_s = (1 - \delta_s) f_s. \tag{44}$$

To estimate γ, the X-ray Transformation is ideally suited. It is closely related to the Radon Transformation and is used to map a function g in $\mathbb{R}^n$ to its integrals over all straight lines in $\mathbb{R}^n$ [26]. Since the range evaluation via (11) produces an image with linear phase progressions along slow-time dimension m for each detection, as shown in Fig. 14(a), this slope can easily be estimated using the suggested X-ray Transformation. However, the estimation accuracy heavily depends on the modulation parameters, e.g. observation time, range and velocity resolution. Note that γ is identical for every detection of the same radar frame. The measurement of a CR at $R = 4.9$ m with 10 MHz coupled setup shown in Fig. 14(a) is artificially induced with an SFO of $f_{SFO} = 1$ MHz. The resulting Rv plot without the SFO correction is shown in Fig. 14(b). Using the method introduced above, the SFO estimation resulted in $f_{SFO,est} \approx 0.9989$ MHz.

Subsequently, the time-domain signal is resampled accordingly. Since values for f_{SFO} are usually very small compared to f_s, a fractional delay filter using Farrow structures is applied [27]. The result is shown in Fig. 15. Compared to before, the peak is sharper and the SNR much higher. Although the velocity offset cannot be corrected via resampling, it is accounted for in the correction method for a CFO.

B. CARRIER FREQUENCY OFFSET & SYMBOL TIMING OFFSET

The estimation of a CFO or STO is done by exploiting the symmetry of the induced error. For a single bistatic channel, the signs of the shifts caused by a CFO and STO are inverse for the two receivers.

The measurement setup introduced in Section III consists of only a single unidirectional channel. Therefore, two separate measurements of a CR at $R = 4.9$ m with a 10 MHz coupled
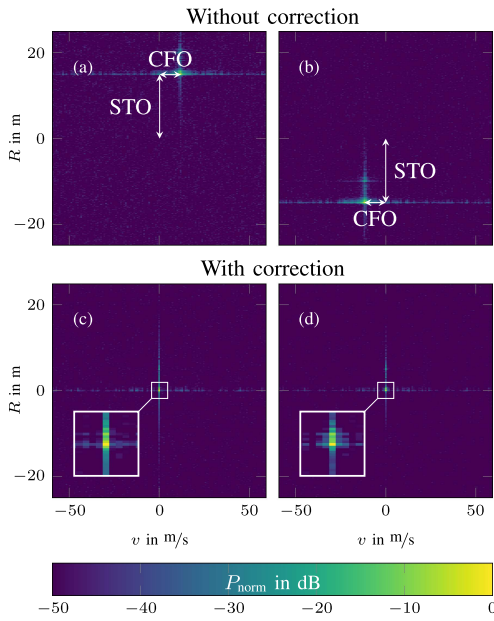
FIGURE 16. Two separate measurements of a CR at $R = 4.9$ m with 10 MHz coupling and artificially induced $f_{CFO} = 6$ kHz and $\Delta t_0 = 100$ ns. The sign of the induced errors is flipped in (a) and (b). Figures (c) and (d) show the corrected Rv plots of the corresponding faulty Rv plots in (a) and (b).

setup are performed. For each measurement, a CFO with $f_{CFO} = 6$ kHz and an STO with $\Delta t_0 = 100$ ns is artificially induced. In-between measurements, the sign of the errors is inverted to simulate the symmetric properties of the range and velocity shifts. The two resulting Rv plots are shown in Fig. 16(a) and (b) respectively.

To circumvent the computational complexity of a 2D-cross-correlation of large Rv images as performed in [18], the problem is reduced to two 1D-cross-correlations. By column- or row-wise summarization, the total velocity or range profile is obtained. The cross-correlation of the two total range profiles gives the range offset, which yields the STO

$$T_{STO,est} = \frac{2R_{est}}{c_0} \approx 100.135 \text{ ns.} \tag{45}$$

Cross-correlation of the two total velocity profiles gives the velocity offset, which is used to calculate the CFO

$$f_{CFO,est} = \frac{2v_{est}f_c}{c_0} \approx 6.00996 \text{ kHz.} \tag{46}$$

The CFO correction is done in time domain by multiplying a carrier signal with frequency $f_{CFO,est}$, while the STO correction is realised by cyclic shifts of the time domain signal. For shifts smaller than one sample, a fractional delay filter using Farrow structures is applied. The resulting Rv images after correction are shown in Fig. 16(c) and (d) respectively. The peaks appear sharper and at the correct location $R = 0$ m and $v = 0$ m/s.

IX. CONCLUSION

Insufficient coherency between uncoupled digital radar sensors leads to a loss in bistatic performance due to SFO, CFO,

PN and STO. Without knowledge of the required level of synchronization, the design of digital radar networks is difficult and often results in the use of complex and costly RF signal distribution networks. With the synchronization criteria derived in this paper, the maximum allowed SFO, CFO and STO can be estimated beforehand, therefore ensuring coherent signal processing of bistatic radar network measurements. Additionally, with the error estimation and correction methods proposed in this work, existing coupling-induced errors are successfully mitigated. Using an X-ray Transformation on faulty range profiles, an SFO is estimated and corrected by resampling the Rx signal. Any CFO and STO is estimated simultaneously by two 1D-cross-correlations of Rv images. The subsequent correction is done in time domain. Since both methods use standard radar images for error estimation, the concepts are applicable to other modulation types used for digital radars.

The presented measurements show the performance degradation caused by coupling-induced errors of digital radar networks and validate the derived criteria. By fulfilling all criteria, the measurement performance of an uncoupled digital radar network is close to the LF coupled measurements. Furthermore, relaxed criteria are proposed and are to be used with the aforementioned signal processing-based synchronization methods. As measurements show, they offer the possibility of coherent bistatic measurements for uncoupled radar networks while removing the need for a very stringent synchronization.

REFERENCES

[1] C. Waldschmidt, J. Hasch, and W. Menzel, "Automotive Radar — From first efforts to future systems," *IEEE J. Microwaves*, vol. 1, no. 1, pp. 135–148, Jan. 2021.

[2] J. Kanz, A. Grathwohl, and C. Waldschmidt, "Surface clutter analysis for detectability prediction of buried objects with a UAV-Based GP-SAR," in *Proc. IEEE 20th Eur. Radar Conf.*, 2023, pp. 221–224.

[3] C. Sturm and W. Wiesbeck, "Waveform design and signal processing aspects for fusion of wireless communications and radar sensing," *Proc. IEEE*, vol. 99, no. 7, pp. 1236–1259, Jul. 2011.

[4] L. G. d. Oliveira, M. B. Alabd, B. Nuss, and T. Zwick, "An OCDM radar-communication system," in *Proc. IEEE 14th Eur. Conf. Antennas Propag.*, 2020, pp. 1–5.

[5] C. Li, V. M. Lubecke, O. Boric-Lubecke, and J. Lin, "A review on recent advances in doppler radar sensors for noncontact healthcare monitoring," *IEEE Trans. Microw. Theory Techn.*, vol. 61, no. 5, pp. 2046–2060, May 2013.

[6] Z. Geng, "Evolution of netted radar systems," *IEEE Access*, vol. 8, pp. 124961–124977, 2020.

[7] M. Gottinger et al., "Coherent automotive radar networks: The next generation of radar-based imaging and mapping," *IEEE J. Microwaves*, vol. 1, no. 1, pp. 149–163, Jan. 2021.

[8] D. Werbunat et al., "Multichannel repeater for coherent radar networks enabling high-resolution radar imaging," *IEEE Trans. Microw. Theory Techn.*, vol. 72, no. 5, pp. 3247–3259, May 2024.

[9] R. Prophet, H. Stark, M. Hoffmann, C. Sturm, and M. Vossiek, "Adaptions for automotive radar based occupancy gridmaps," in *Proc. IEEE MTT-S Int. Conf. Microw. Intell. Mobility*, 2018, pp. 1–4.

[10] T. Grebner, R. Riekenbrauck, and C. Waldschmidt, "Simultaneous localization and mapping (SLAM) for synthetic aperture radar (SAR) processing in the field of autonomous driving," *IEEE Trans. Radar Syst.*, vol. 2, pp. 47–66, 2024.

[11] M. Gottinger, P. Gulden, and M. Vossiek, "Coherent signal processing for loosely coupled bistatic radar," *IEEE Trans. Aerosp. Electron. Syst.*, vol. 57, no. 3, pp. 1855–1871, Jun. 2021.

[12] A. Dürr, D. Böhm, D. Schwarz, S. Häfner, R. Thomä, and C. Waldschmidt, "Coherent measurements of a multistatic MIMO radar network with phase noise optimized non-coherent signal synthesis," *IEEE J. Microwaves*, vol. 2, no. 2, pp. 239–252, Apr. 2022.

[13] D. Werbunat, B. Meinecke, B. Schweizer, J. Hasch, and C. Waldschmidt, "OFDM-Based radar network providing phase coherent DOA estimation," *IEEE Trans. Microw. Theory Techn.*, vol. 69, no. 1, pp. 325–336, Jan. 2021.

[14] G. Krieger and A. Moreira, "Spaceborne bi- and multistatic SAR: Potential and challenges," *IEE Proc. Radar, Sonar Navig.*, vol. 153, no. 3, pp. 184–198, 2006.

[15] A. Grathwohl, B. Meinecke, M. Widmann, J. Kanz, and C. Waldschmidt, "UAV-Based bistatic SAR-Imaging using a stationary repeater," *IEEE J. Microwaves*, vol. 3, no. 2, pp. 625–634, Apr. 2023.

[16] V. Janoudi et al., "Antenna array design for coherent MIMO radar networks," in *Proc. IEEE Radar Conf.*, 2023, pp. 1–6.

[17] A. Durr, B. Schneele, D. Schwarz, and C. Waldschmidt, "Range-angle coupling and near-field effects of very large arrays in mm-wave imaging radars," *IEEE Trans. Microw. Theory Techn.*, vol. 69, no. 1, pp. 262–270, Jan. 2021.

[18] V. Janoudi, P. Schoeder, T. Grebner, N. Appenrodt, J. Dickmann, and C. Waldschmidt, "Signal model for coherent processing of uncoupled and low frequency coupled MIMO radar networks," *IEEE J. Microwaves*, vol. 4, no. 1, pp. 69–85, Jan. 2024.

[19] D. Werbunat et al., "On the synchronization of uncoupled multistatic PMCW radars," *IEEE Trans. Microw. Theory Techn.*, early access, Feb. 07, 2024, doi: 10.1109/TMTT.2024.3359035.

[20] C. Sturm, E. Pancera, T. Zwick, and W. Wiesbeck, "A novel approach to OFDM radar processing," in *Proc. IEEE Radar Conf.*, 2009, pp. 1–4.

[21] G. Hakobyan and B. Yang, "A novel intercarrier-interference free signal processing scheme for OFDM radar," *IEEE Trans. Veh. Technol.*, vol. 67, no. 6, pp. 5158–5167, Jun. 2018.

[22] R. F. Tigrek, W. J. A. De Heij, and P. Van Genderen, "OFDM signals as the radar waveform to solve doppler ambiguity," *IEEE Trans. Aerosp. Electron. Syst.*, vol. 48, no. 1, pp. 130–143, Jan. 2012.

[23] R. F. Tigrek and P. Van Genderen, "Compensation of range migration for cyclically repetitive Doppler-sensitive waveform (OFDM)," *IEEE Trans. Aerosp. Electron. Syst.*, vol. 46, no. 4, pp. 2118–2123, Oct. 2010.

[24] B. Schweizer, D. Schindler, C. Knilll, J. Hasch, and C. Waldschmidt, "On hardware implementations of stepped-carrier OFDM radars," in *Proc. IEEE/MTT-S Int. Microw. Symp.*, 2018, pp. 891–894.

[25] L. Smaini, *RF Analog Impairments Modeling for Communication Systems Simulation: Application to OFDM-Based Transceivers*. Hoboken, NJ, USA: Wiley, Aug. 2012.

[26] P. Maass, "The x-ray transform: Singular value decomposition and resolution," *Inverse Problems*, vol. 3, no. 4, pp. 729–741, Nov. 1987.

[27] T. Hentschel and G. Fettweis, "Continuous-time digital filters for sample-rate conversion in reconfigurable radio terminals," *Frequenz*, vol. 55, no. 5/6, pp. 185–188, May 2001.

JULIAN AGUILAR (Graduate Student Member, IEEE) received the M.Sc. degree in electrical engineering from Ulm University, Ulm, Germany, in 2022, where he is currently working toward the Ph.D. degree in electrical engineering with the Institute of Microwave Engineering. His research interests include digital radar systems in the automotive sector, and the accompaning signal processing.

DAVID WERBUNAT (Graduate Student Member, IEEE) received the B.Sc. and M.Sc. degrees in electrical engineering from Ulm University, Ulm, Germany, in 2017 and 2019, respectively, where he is currently working toward the Ph.D. degree with the Institute of Microwave Engineering. His research interests include digital radar systems, system concepts, synchronization methods, and signal processing for uncoupled coherent radar networks. He was the recipient of 2021 VDE ITG Prize for his outstanding work on OFDM-based radar networks. He was also the recipient of first place in the IMS Advanced Practice Paper Competition in 2023.

VINZENZ JANOUDI (Graduate Student Member, IEEE) received the M.Sc. degree in electrical engineering from the University of Applied Sciences of Karlsruhe, Karlsruhe, Germany, in 2018, and the M.Eng. degree from Toronto Metropolitan University, Toronto, ON, Canada, in 2019. He is currently working toward the Ph.D. degree in electrical engineering with the Institute of Microwave Engineering, Ulm University, Ulm, Germany.

CHRISTINA (KNILL) BONFERT (Member, IEEE) received the Dr.-Ing. degree in electrical engineering from Ulm University, Ulm, Germany, in 2021. From 2015 to 2021, she was a Research Assistant with the Institute of Microwave Engineering, Ulm University, where her doctoral research was focused on orthogonal frequency-division multiplexing radar, novel digital radar signal processing methods, and signal design for digital radars. Since 2022, she has been a Postdoctoral Researcher with the Institute of Microwave Engineering, Ulm University. Her research interests include signal processing and compressed sensing for UAV-based synthetic aperture radar systems and applications. Dr. Bonfert was the Co-Chair of the European Radar Conference in 2023.

CHRISTIAN WALDSCHMIDT (Fellow, IEEE) received the Dipl.-Ing. (M.S.E.E.) and Dr.-Ing. (Ph.D.E.E.) degrees from the University of Karlsruhe, Karlsruhe, Germany, in 2001 and 2004, respectively. From 2001 to 2004 he was a Research Assistant with the Institut für Höchstfrequenztechnik and Elektronik, Universität Karlsruhe, Karlsruhe, Germany. Since 2004, he has been with Robert Bosch GmbH, Gerlingen, Germany, working on the business units Corporate Research and Chassis Systems. He was heading different research and development teams in microwave engineering, RF-sensing, and automotive radar. In 2013, he returned to academia. He was appointed as the Director of the Institute of Microwave Engineering, University Ulm, Ulm, Germany, as a Full Professor. He has authored or coauthored more than 320 scientific publications and more than 25 patents. His research interests include radar and RF-sensing, mm-wave and submillimeter-wave engineering, antennas and antenna arrays, and RF and array signal processing. Dr. Waldschmidt is a member of the Executive Committee Board of the German MTT/AP Joint Chapter and the German Information Technology Society. He was the Chair of the IEEE MTT-29 Technical Committee on Microwave Aerospace Systems and MTT-27 Technical Committee on Wireless Enabled Automotive and Vehicular Applications. He was a two-time TPC Chair and the General Chair of the IEEE MTT International Conference on Microwaves for Intelligent Mobility. He was the General Chair of the German Microwave Conference in 2022 and General Chair of the European Radar Conference in 2023. He was a three-time Guest Editor of *IEEE Microwave Magazine* and IEEE MICROWAVE AND WIRELESS COMPONENTS LETTERS. From 2018 to 2022, he was an Associate Editor for IEEE MICROWAVE AND WIRELESS COMPONENTS LETTERS. He is a reviewer of multiple IEEE Transactions and many IEEE conferences in the field of microwaves. He was the co-recipient of more than 15 best paper awards. Since 2020, he has been a member of the Heidelberg Academy of Sciences and Humanities.